University of Bristol - Explore Bristol Research
General rights
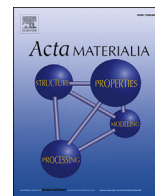
Full length article

An Atom Probe Tomography study of site preference and partitioning in a nickel-based superalloy

P.A.J. Bagot [a, *], O.B.W. Silk [a], J.O. Douglas [a], S. Pedrazzini [a], D.J. Crudden [a], T.L. Martin [a], M.C. Hardy [b], M.P. Moody [a], R.C. Reed [a]

[a] Department of Materials, University of Oxford, Parks Road, Oxford OX1 3PH, UK
[b] Rolls-Royce plc, Elton Road, Derby DE24 8BJ, UK

ARTICLE INFO

ABSTRACT

Atom Probe Tomography (APT) has been utilised for an in-depth examination of the commercial poly-crystalline Ni-based superalloy RR1000, assessing compositions of the primary, secondary and tertiary γ' phases. Clear differences in the phase chemistries are noted, particularly for the tertiary γ' to which much of the alloy strength is attributed. Trace amounts of Hf are found to segregate strongly to the primary and secondary γ' phases, but also exhibit an extended diffusion profile across the γ-γ' interface up to 80 nm wide. Ti, Al and Mo demonstrate similar, yet not as pronounced diffusion profiles, indicating assumed phase chemistries may not be representative of those regions adjacent to the γ-γ' interface. Within γ', unique element site-occupancy preferences for this alloy were identified. Finally, the grain boundary chemistry across a γ-γ interface and that of an intragranular boride were analysed, identifying the latter as a mixed M_5B_3 boride rich in Mo and Cr. These demonstrate further the depth of information on Ni-alloys accessible by APT, while the overall implications of results in comparison with other in-service/model alloys are also discussed.

1. Introduction

Where do the atoms in an alloy reside? This question is of fundamental importance to the field of materials science and the discipline of physical metallurgy from which it emerged. Unfortunately, for structural alloys — which are usually based upon one of Al, Fe, Ni or Ti — truly unequivocal answers are not yet available. One explanation for this is complexity. These alloys are usually multicomponent in nature with many alloying elements added. Strengthening phases are nearly always present, and these can be ordered, so that a site preference arises. Moreover, precipitate distributions are often multimodal. Alloys are mainly poly-crystalline, so that segregation and/or grain boundary precipitation can arise. To what extent can a modern high-resolution character-isation techniques answer this critical question?

The nickel-based superalloys are a class of structural alloy for which the above description of complexity is particularly appro-priate. First, these are multicomponent alloys with ten or more alloying elements present; arguably they represent some of the most complex alloys designed by man. An ordered strengthening phase, based upon the $L1_2$ crystal structure, plays an important role in the alloy microstructure; thus preferential partitioning of ele-ments is expected not only to this phase but also to the sub-lattice atomic sites within it. Elements such as B and C are added which are known to segregate to grain boundaries [1,2], however the extent of this segregation and whether secondary phases such as carbides and borides form as a result remains unclear. Finally, elements such as Hf and Zr are sometimes added in trace quantities for a variety of intended benefits including gettering sulphur at grain boundaries [3] and to prevent oxide scale spallation [4]; however the mecha-nisms for these are still not well understood. Characterising chemical distribution at the atomic-scale is therefore a key step in developing an understanding of the role of individual elements, their interactions in the microstructure and ultimately the perfor-mance of the material. Increasingly demanding applications for components made from such materials, most notably for jet pro-pulsion [5] and power generation [6], drives continued develop-ment of these alloys to perform in extreme conditions. Detailed characterisation of these materials is essential to enable such progress.

In this study, the modern high-strength polycrystalline nickel-based superalloy RR1000, an alloy developed by Rolls-Royce plc, is subjected to detailed high resolution analysis using atom probe tomography (APT). Due to the complex chemistry of this alloy, a technique is needed which is capable of resolving the numerous components with equal sensitivity, whilst providing the spatial resolution needed to map microstructures of the differently sized phases. APT complements more conventional analyses such as electron microscopy [7–9] and X-ray/neutron scattering [10,11]. Examples of insights provided by APT into these types of alloys have been previously reviewed [12,13], while focussed studies include composition-dependent interactions between solutes [14], evolution of lattice spacings and precipitates during ageing [15,16], informing dislocation-precipitation interaction simulations [17], behaviours of individual solute elements including Re [18–20], Pt-group metals [21–24], Nb [25], segregation at grain boundaries [1,26,27] and oxidation around crack tips [28,29]. For the newly discovered class of Co-based alloys, APT has also been used effectively to investigate chemical partitioning and the nature of certain microstructural features [30–32].

RR1000 is in use in current generation aero engine components such as high-pressure turbine discs. Despite the extensive use of APT to look at various model and commercially-used superalloys, few detailed studies have been published on RR1000 or similar alloys using this technique. Therefore, we examine in detail element partioning behaviour and inter-relationships in the γ' phases of this alloy, and assess how specific elements segregate to grain boundaries. The latter is becoming increasingly important in disc alloys required to operate for longer periods at elevated temperatures in modern flight paths, leading to rising concerns over creep and low cycle fatigue characteristics [33].

2. Experimental

Samples of RR1000 were provided by Rolls-Royce plc. This alloy was manufactured using powder metallurgy, and following hot isostatic pressing and recrystallization during extrusion it was isothermally forged to shape. After a solution heat treatment at 1120 °C (sub-solvus) for 4 h, it was air-cooled then precipitation aged at 760 °C for 16 h to yield a fine-grained (~5 μm average dia.) microstructure.

For optical and electron microscopy, samples were cut from the as-received material using an ISOMET™ 5000 precision saw. These were successively ground using a series of SiC grit papers before being diamond polished to a final 1 μm surface roughness finish, then colloidal silica polished up to 0.04 μm finish. Samples prepared in this manner were analysed using a combination of Zeiss NVision 40, Zeiss Merlin and JEOL 6500 Scanning Electron Microscopes (SEM), varying the voltage between 5 and 15 kV to suit the signal-to-noise requirements of different high resolution secondary and backscattered electron micrographs. Energy Dispersive X-ray Spectroscopy (EDX) was performed on selected areas of the samples in a Zeiss Merlin SEM equipped with two Oxford Instruments detectors and Aztec software. Separate samples for optical/SEM studies were etched in 10 vol% orthophosphoric acid in H_2O at 10 V for 5–10 s to preferentially dissolve the γ matrix.

For APT analysis, matchsticks (0.5 × 0.5 × 15 mm) cut from the alloy were initially electropolished in a 10 vol% perchloric acid/acetic acid solution, then finished in a solution of 2 vol% perchloric acid in butoxyethanol to suitably sharp needle-shaped samples. To examine grain boundaries and site-specific regions, bulk samples mechanically polished as described above were utilised to prepare needles by the lift-out procedure [34] using a Zeiss NVision dual-beam FIB, taking care to minimize Ga^+ beam-damage with a final 2 kV/30 pA polish. APT data was collected using a Cameca LEAP™

3000X HR instrument in the Department of Materials, University of Oxford. The majority of samples were run in voltage mode at a specimen temperature of 50 K, with 200 kHz pulses at a pulse fraction of 20%. The small subset of potentially more fragile samples containing grain boundaries were run in laser mode, with pulse energies of 0.2–0.6 nJ.

3. Results

3.1. SEM/EDX

Fig. 1a–b shows SEM secondary electron micrographs of the etched RR1000 microstructure at two different magnifications. Together these figures reveal a trimodal size distribution of γ' precipitates and their relative location in the microstructure. The largest (>500 nm) primary γ' precipitates are the least prevalent, located along grain boundaries, as indicated in Fig. 1a). The secondary γ' (~250 nm in size) are the most abundant by volume fraction, while the smallest tertiary γ' ($\leq$50 nm) precipitates appear uniformly distributed but are most easily visible at grain boundaries.

Also highlighted in Fig. 1a is the presence of two intragranular precipitates. Fig. 1c) isolates these at high magnification, along with a series of EDX maps identifying them as a Mo-Cr rich boride and a smaller Ta-Hf rich carbide. These were not observed within every grain. Some borides also appeared enveloped within a γ' shell. Site-specific APT analysis, enabled by FIB lift-out specimen preparation, was undertaken to more precisely examine the composition of the larger intragranular borides, as discussed below.

Smaller elongated borides (approximately 1/10th the size of intragranular borides) were also noted infrequently along grain boundaries; most boundaries examined however were boride free. Furthermore etching of samples to expose phases reduces EDX resolution through creation of surface topographical features. These can partly shield the signal making smaller particles challenging to identify. However the composition of the smaller borides appeared very similar to that of the intragranular one shown in Fig. 1, enriched in Mo and Cr.

3.2. Atom Probe Tomography

APT analysis across numerous samples, comprising 35 million ions in total, provided a measurement of the overall alloy composition, in Table 1, with sufficient sensitivity to detect all minor alloying elements. The measured concentrations are in close agreement with specified values for the major elemental additions, with the exception of Zr (0.1 at.% nominal). Trace levels of Fe (0.4 at.%) and Si (0.06 at.%) were also identified. The primary γ' phases are retained from sub-solvus processing, whilst the secondary and tertiary γ' phases nucleate during different stages in the cooling [35]. The primary γ' particles, which are the largest, incoherent, and located at the grain boundaries form during alloy solidification, prior to any thermal-mechanical processing. The alloy is then aged below the solvus temperature in order to preserve these, where they act to pin the grain boundaries, inhibiting grain coarsening to create a finer grain size distribution. The secondary and tertiary γ' particles however form during subsequent thermal ageing treatments. An in-depth modelling study on RR1000 [36] has correlated thermal treatments to different size distributions of secondary and tertiary γ', and their relative contributions to the overall strength of the alloy.

Hence, the matrix composition differs relatively for each stage at which these phases respectively form, leading to slightly different γ' chemistries. The chemistries of tertiary γ' precipitates are the most distinct of the three, containing significantly more Mo and Al
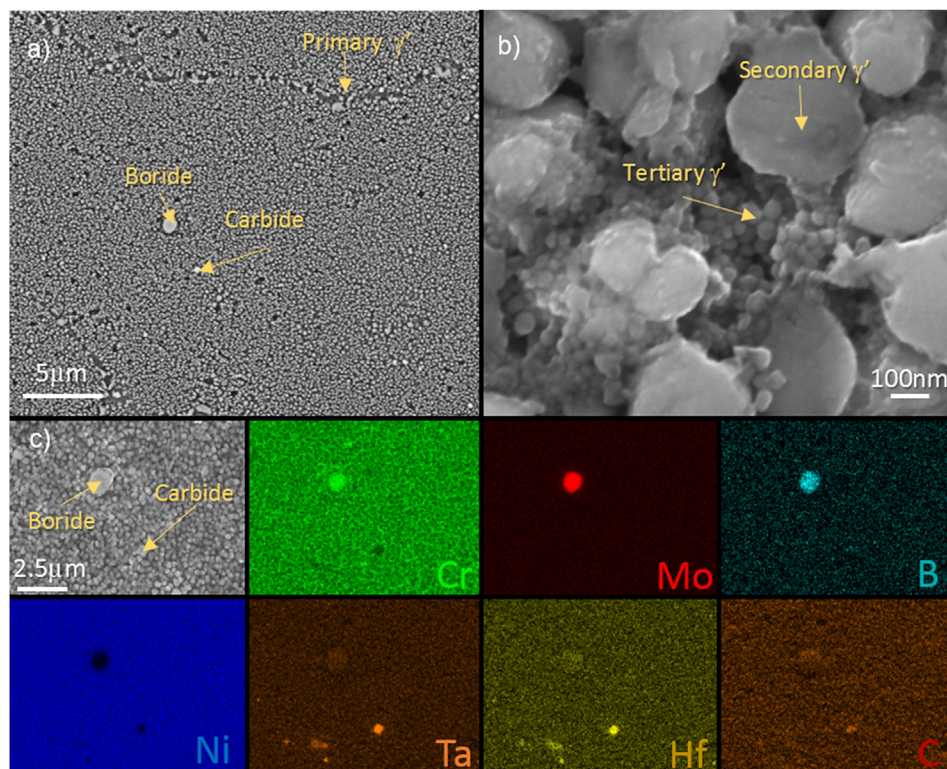
Fig. 1. a) SEM Secondary Electron micrograph of etched RR1000 microstructure with labelled grain boundary primary γ′ phase, an intragranular (Ta-Hf rich) carbide and (Mo-Cr rich) boride. b) High magnification view of secondary and tertiary γ′. c) Close-up of isolated carbide/boride and corresponding EDX maps showing elemental compositions.

Table 1
Compositions of overall alloy (combined datasets), primary, secondary, tertiary γ′ and matrix, along with nominal specification.

at.%	Ni	Cr	Co	Mo	Al	Fe	Ti	B	Ta	Hf
Nominal	50.9	16.5	17.9	3	6.35	–	4.3	0.08	0.63	0.16
Overall	49.6	17.6	18.0	3.24	6.19	0.39	4.00	0.06	0.54	0.13
Primary γ′	67.2	1.28	6.55	0.75	12.3	0.09	9.32	0.04	1.41	0.25
Secondary γ′	67.7	1.41	6.68	0.74	11.6	0.03	9.51	0.04	1.43	0.37
Tertiary γ′	67.4	1.48	6.07	1.66	14.2	0.07	7.71	0.06	0.88	0.03
Matrix	36.0	30.1	26.3	4.84	1.46	0.66	0.26	0.08	0.03	–

at the expense of Ti, Ta and Hf.

The chemical partitioning into the various γ′ phases for selected major elements is visualised in the atom maps in Fig. 2. These
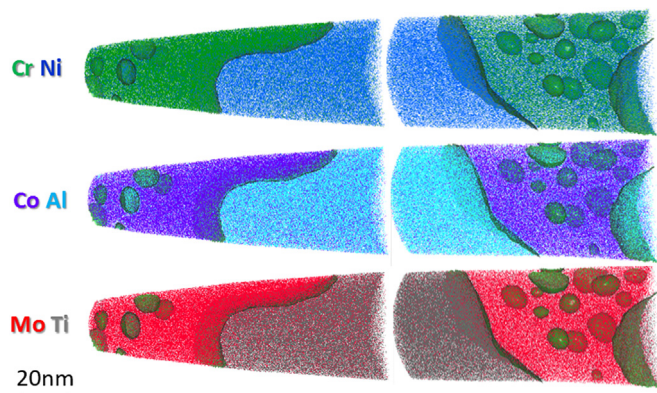

Fig. 2. Atom maps showing distribution of selected major species, along with secondary/tertiary γ′ precipitates demarcated using Cr 7 at.% isosurfaces.

highlight the curved secondary γ′-γ interfaces also apparent in the SEM images. It is evident that the tertiary γ′ precipitates are approximately spherical, but with a range in sizes. In APT, regions containing a higher or lower concentration of a particular element can be highlighted by the application of iso-concentration surfaces onto the atom map. In Fig. 2 an iso-concentration defining regions containing more than 7 at.% Cr is applied to demarcate all γ-γ′ interfaces and in particular highlight the presence, size and shape of the tertiary γ′ precipitates. Iso-concentration regions were also used to isolate the different regions of the microstructure that they define and enable accurate measurement of the composition of each feature, as presented in Table 1. The 7 at.% Cr surface used for these analyses is a relatively conservative value, defining a position of the tertiary γ′-γ interface closer to the centre of γ′ precipitate. Although this definition will slightly underestimate average tertiary γ′ sizes, it ensures the accuracy of the measured precipitate chemistries, particularly for the smallest ones. Using this approach an average radius of 5.4 ± 2.1 nm was determined for all tertiary γ′ precipitates fully encapsulated in the APT reconstruction.

The Ni_3Al basic structure of γ′ phase in a binary Ni-Al system contains Ni atoms in the fcc sublattice sites (α) and Al atoms in the corner sublattice ones (β). In the more complex RR1000 alloy, γ′ chemistry at equilibrium is assumed to take the form of (Ni,Cr,-Co,Mo)$_3$(Al,Ti,Ta,Hf). From the APT data, the mean value of the α:β ratio is 3.3 ± 0.2:1 in the tertiary γ′, somewhat higher than that the nominal value of 3:1 predicted by assumed stoichiometry. The secondary γ′ phase has an identical ratio of 3.3:1, while in the primary γ′ it is 3.2:1. All these suggest that the predicted model stoichiometry is therefore somewhat oversimplified in this alloy.

Determining phase chemistries also allows calculation of the γ′ volume fraction $\phi_{\gamma'}$, a major design parameter in disc-alloys but one which can be difficult to verify experimentally by conventional techniques. It can be calculated using the Lever rule:

$$C_n = \phi_{\gamma'} C_{\gamma'} + \left(1 - \phi_{\gamma'}\right) C_{\gamma'}$$

where C_n, $C_{\gamma'}$ and C_{γ} are the concentrations of each alloy species in the overall material, γ' and γ phases respectively. A plot of C_n-C_{γ} vs. $C_{\gamma'}$-C_{γ} should yield a straight line with gradient equal to $\phi_{\gamma'}$, as shown in Fig. 3. From this the γ' volume fraction is 43 at.% (42 wt%), determined using the secondary γ' chemistries which dominate the microstructure. This is in reasonable agreement with a design expectation of 45−48 wt%.

The elemental partitioning behaviour across the primary, secondary and tertiary γ'-γ interfaces, respectively, are investigated by means of proximity histogram analyses presented in Fig. 4a−f. Proximity histograms are a measure of phase chemistry as a function of distance from an interface as defined by an iso-concentration surface. In the case of the tertiary γ', because of the small surface areas of each single precipitate interface, the histogram is generated using data averaged over many precipitates to improve statistical analysis. For the main alloying elements, the proximity histogram profiles are very similar across all three precipitate-matrix interfaces, typically less than 2 nm in width. However, some species do show significantly different behaviour; approaching the interface from within the γ' phases, the Ti and Ta levels fall, while both Mo and Al contents rise slightly in all precipitate types.

The distribution of Hf across the primary and secondary γ'-γ interfaces has a much more extended profile shape. In Fig. 5a a cylindrical region of interest (diameter 15 nm and length 135 nm) is defined, oriented perpendicular to the interface to examine the Hf atomic distribution profile at the maximum possible distances from it. The size of displayed Hf atoms in Fig. 5a has been increased for visual clarity. The resulting concentration profile as measured over this length is shown in Fig. 5b. This highlights a continued increase in Hf concentration on moving into the γ' phase up to ~80 nm away from the interface, ultimately reaching a maximum of approximately 0.6 at.%. While Fig. 5 represents measurement of a specific secondary γ'-γ interface, the Hf proximity histograms in Fig. 4b) and d) suggest very similar behaviour in both primary and secondary γ'. Hf partitions very strongly to both these phases, present at nearly 3.8 times the nominal alloy content.

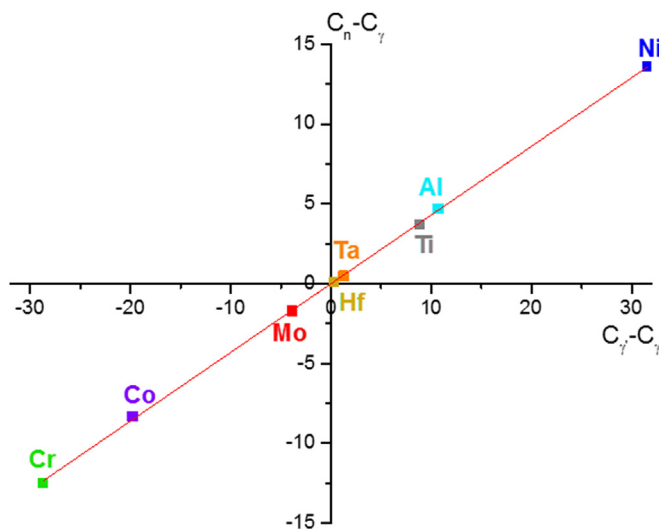In certain volumes within the APT reconstruction the spatial

resolution is sufficient to observe crystallographic planes perpendicular to the analysis direction throughout the specimen depth. For γ' phases, where the analysis direction and $\langle 100 \rangle$ crystal direction closely aligned, it was possible to produce spatial distribution maps (SDMs) [37,38], effectively 1D distribution profiles along a specific crystallographic direction, revealing site-occupancies of different elements within the ordered phase. SDM analyses for a secondary γ' phase are presented in Fig. 6, plotting the distribution of solutes relative to the position of the Ni atoms. Each graph in this figure is generated by examining the local neighbourhood around each individual Ni atom, building a frequency distribution of the relative separation in the <100> direction of the surrounding atoms. The dotted vertical lines mark positions of the β-lattice sites in the intermetallic γ'. It is apparent from the peak heights that Al, Ti, Ta, Mo (to a lesser extent) and Hf prefer to reside on the β-lattice sites. The Hf data is also visualised in the close-up slice through an atom map of Fig. 6c. In contrast, Co and Cr favour the α-lattice sites. Similar results were obtained in the site-occupancy analysis of the tertiary γ' phase, although the diminished statistics due to smaller numbers of atoms in these inevitably leads to much less distinct peaks in SDMs. The primary γ' phase was only examined through a separate targeted lift-out which did not reveal a suitable lattice structure for site occupancy analysis.

3.3. Grain boundary/boride analysis

The alloy chemistry at a grain boundary was examined, Fig. 7, highlighting a randomly selected γ-γ grain boundary. Also indicated on the atom map is a cylindrical region of interest perpendicular to and intersecting this grain boundary. A 1D elemental concentration profile measurement through the length of this cylinder and crossing the boundary is displayed in Fig. 7b. The profile shows a marked change in chemistry at the grain boundary, with strong segregation of Mo and B, and slight enrichment of Cr and C. Quantification of the enrichment of these elements was estimated using the Gibbsian interfacial excess (Γ) [39]. Values of Γ (in atoms/nm^2) determined were 11.0 ± 0.2 (Mo), 2.7 ± 0.8 (Cr), 5.6 ± 0.6 (B), 0.6 ± 0.3 (C). It is important to note that the exact levels of segregation will depend on the character of the grain boundary, for which dedicated EBSD-based methods are additionally required for APT specimen preparation (e.g. Ref. [40]), beyond the scope of the current work.

Analysis of the large intragranular precipitate shown by EDX to be a Mo-Cr rich boride yielded a completely homogeneous microstructure (over 2M ions). The composition of this is given in Table 2, confirming the boride has a stoichiometry corresponding closely to M_5B_3. Although this mostly consists of Mo and Cr metals, there are also traces of Ti, Ta, Ni and Co present.

4. Discussion

4.1. Experimental vs. predicted γ' chemistries

To investigate the thermodynamics of different γ' phase formation, ThermoCalc software and the Thermotech Ni-based Superalloys Database (TTNI8) were used to predict γ' composition as a function of temperature. From this data, shown in Fig. 8, results from the two temperatures used in the as-defined heat treatments (1120 °C and 760 °C), can be directly compared with the APT-derived γ' compositions, as displayed in Table 3.

The modelling data shown in Fig. 8 highlights the dependence of γ' phase compositions on temperature, in particular for Ni, Co and Cr. At 1120 °C, predicted concentrations of Al, Ta, Ti, Hf are in good agreement with APT data for the primary and secondary γ' phases (Table 3). In contrast, data for Ni, Co, Cr, Mo match less well,

Fig. 3. Plot of C_n-C_{γ} vs. $C_{\gamma'}$-C_{γ} generated from compositions of selected species in Table 1.
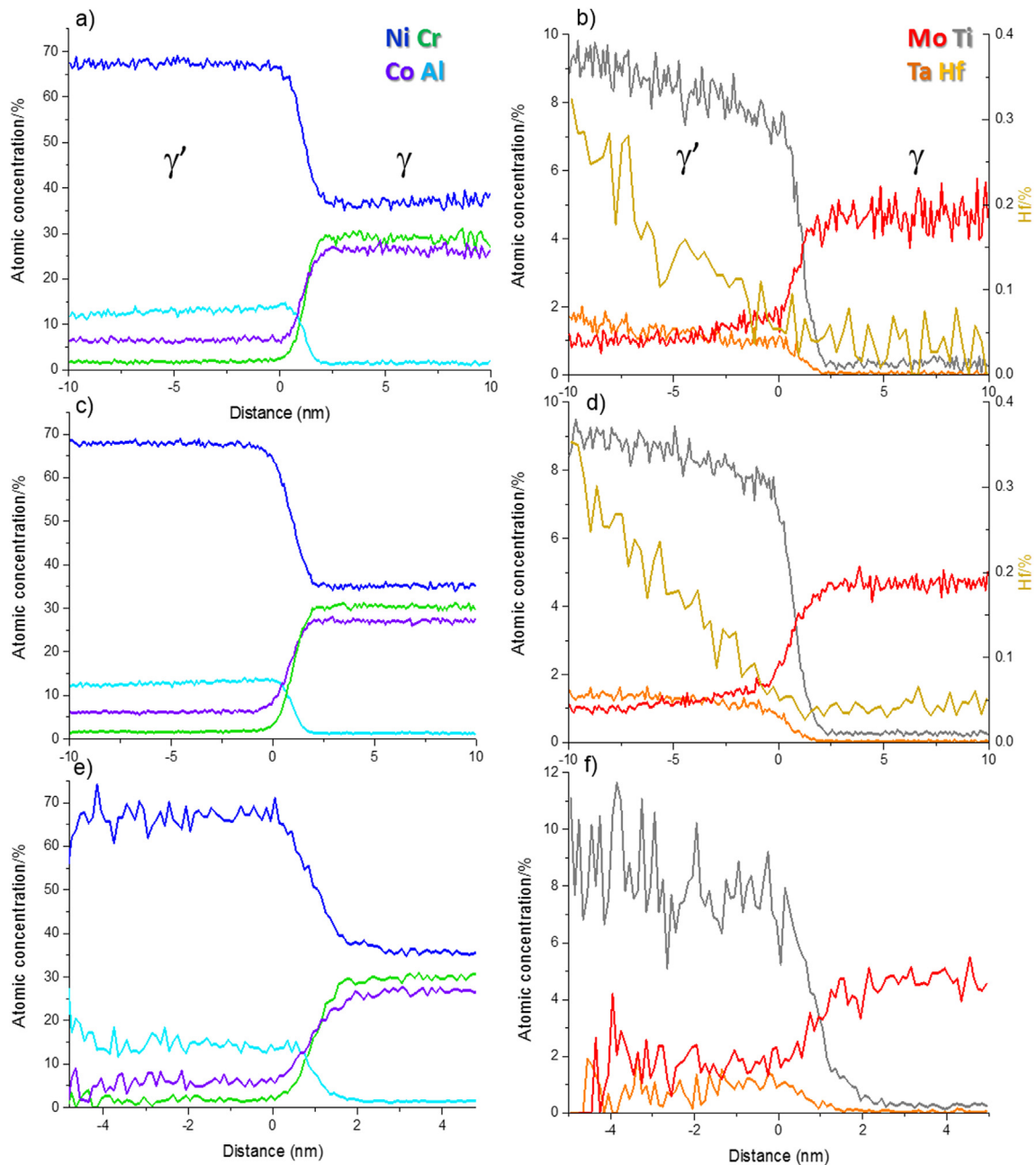
Fig. 4. Proximity histograms across γ−γ′ interfaces for major and minor elements in primary (a–b), secondary (c–d) and tertiary (e–f) γ′ phases. Note separate Hf scaling axis.

estimating around double the levels of Co and Cr (and half that of Mo) as seen experimentally. At an aging temperature of 760 °C, the ThermoCalc prediction is again not in good agreement with the tertiary γ′ data, particularly for Mo, Ti, Ta and Hf. The APT measured level of Mo is over 6 times higher than predicted, while conversely the Hf concentration is 6 times less than the expected value.

The tertiary γ′ precipitates are the most different in chemistry compared to the primary and secondary. These smallest phases strongly influence the alloy strength [41], hence a more detailed understanding of how processing and operational conditions influence their nature is highly desirable. Within the broad range of tertiary γ′ sizes (5.4 ± 2.1 nm) observed by APT, it was of interest to examine possible size-chemistry relationships. The concentration of a single element within one tertiary γ′ precipitate was subject to a considerable degree of scatter, therefore the ratio of combined α-

site species (Ni, Co, Cr, Mo) to β-site ones (Al, Ta, Ti, Hf) was examined. Across individual precipitates ranging in size between 4 and 20 nm, there appeared to be little difference in this ratio. A recent STEM-EDX study on the same alloy [42] also found little variation in composition within each type of γ′ phase, although the ratio shifted in favour of β-site species on moving from tertiary to secondary to primary. However in the STEM-EDX study the chemical resolution was restricted to precipitates ≥20 nm in diameter, while the APT here is able to confirm consistent γ′ chemistries down to nearly 4 nm.

The greatest difference between these two studies is the value of the α:β site species ratio for tertiary γ′, determined to be 3.3 ± 0.2:1 via APT compared to 2.62 ± 0.05:1 using STEM-EDX [42]. Aside from possible quantification limitations by the STEM-EDX method, this may be due to differences in ageing conditions which have been
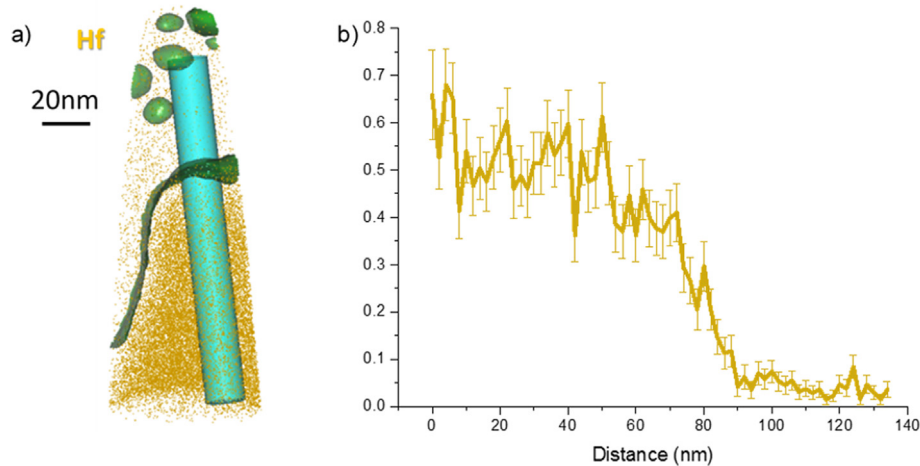
Fig. 5. a) Hf atom map with analysis cylinder, b) resulting 1D concentration profile.
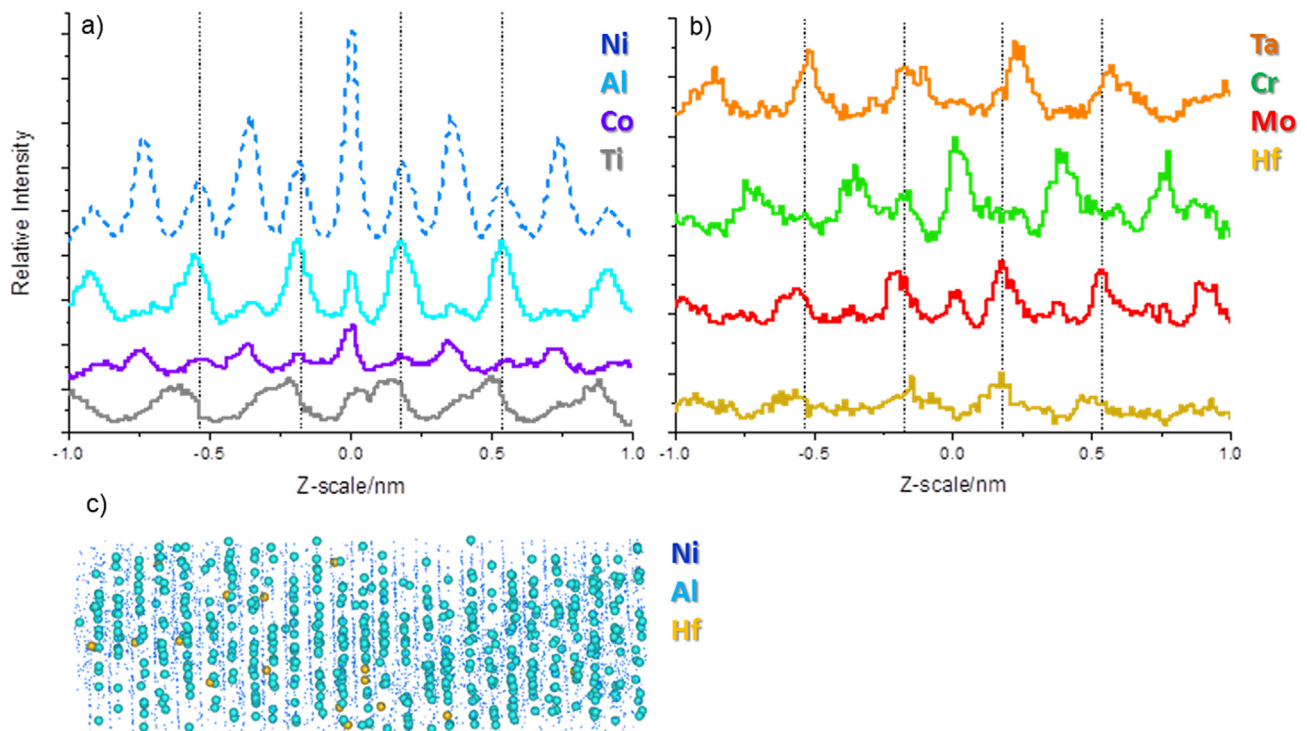

Fig. 6. a), b) Spatial Distribution Maps generated for Ni-X distances in secondary precipitates. Dotted lines indicate positions of β-lattice sites at ±0.179 nm from central reference plane. c) Atom map slice (4 nm dia.) through secondary γ′, showing Ni₃Al lattice structure and Hf atoms on Al lattice sites.

shown to significantly impact phase chemistries. For example in a prior APT study of Rene 88DT [15] excess levels of β-site elements were retained in secondary γ′ phases following insufficient ageing to achieve equilibrium; after even 50 h ageing at 760 °C the Co, Mo and in particular Cr levels in the secondary γ′ were higher than in the primary.

The sublattice preference of Cr (and indeed Co) do not show distinct trends in the existing APT data, an issue underlined by Liu et al. [43]- "It is unclear whether Cr occupies the Ni or Al sublattice sites", while Booth-Morrison et al. [44] state "The site preference of Cr has generally been found to depend on the alloy composition and aging treatment". For RR1000, the one directly comparable prior study on the same alloy by Collins et al. [45] use a combination of XRD and simulated XRD patterns to determine that "Co and Cr will predominantly occupy the Ni sublattice". This is entirely consistent with our own finding − we indeed see Cr mainly occupying the Ni sublattice in Fig. 6, but there is evidence of Cr also on the Al sublattice sites. The overall consensus is that even slight changes in composition can affect this preference and that Cr can be particularly influenced as it "only weakly" prefers the Al sublattice sites in a model Ni-Al-Cr-Ta alloy, as determined using first-principles calculations [44].

4.2. Interfacial effects and role of hafnium

The STEM-EDX study identified Hf only in the primary γ′ precipitates, enriched to 0.66 at.% [42]. In comparison APT confirms that Hf is present in both the primary and secondary γ′ precipitates,
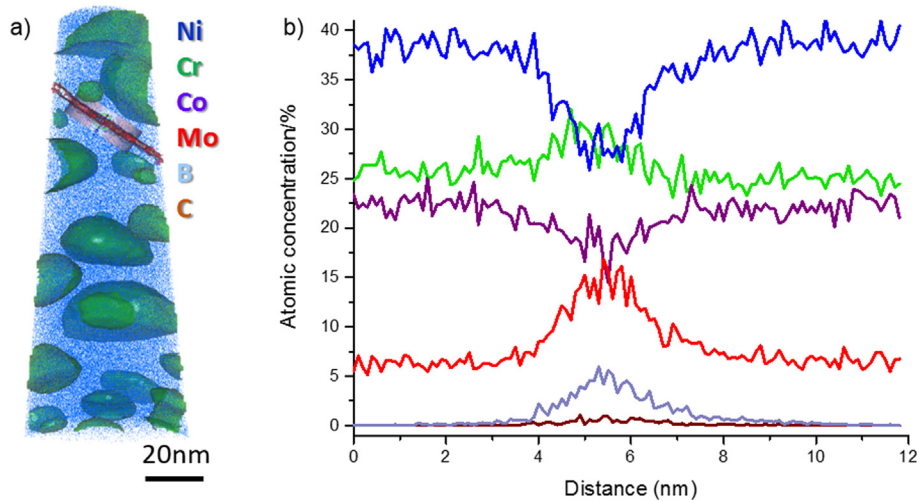
Fig. 7. a) Atom map containing grain boundary, as marked using Mo 8.9% isosurfaces. Also marked is analysis cylinder for extraction of 1D concentration profile of selected species in b).

Table 2
Composition (in at.%) of species located at intragranular boride in RR1000.

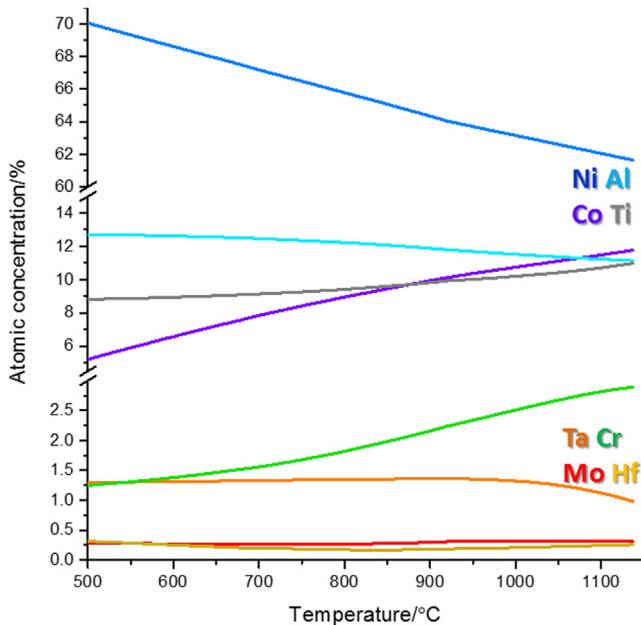| B	Mo	Cr	Ti	Co	Ni	Ta
35.9	33.8	22.0	2.6	2.2	1.9	1.2

Fig. 8. ThermoCalc prediction of RR1000 equilibrium composition as function of temperature.

Table 3
Thermocalc-predicted/APT-determined γ' compositions for selected elements.

at.%	Ni	Cr	Co	Mo	Al	Ti	Ta	Hf
Thermocalc @ 1120 °C	61.9	2.86	11.6	0.31	11.2	10.8	1.05	0.25
Thermocalc @ 760 °C	66.4	1.70	8.51	0.26	12.3	9.29	1.34	0.18
Primary γ'	67.2	1.28	6.55	0.75	12.3	9.32	1.41	0.25
Secondary γ'	67.7	1.41	6.68	0.74	11.6	9.51	1.43	0.37
Tertiary γ'	67.4	1.48	6.07	1.66	14.2	7.71	0.88	0.03

at a very similar level of 0.6 at.%. An extended Hf concentration profile was observed in both primary and secondary γ' phases, with negligible Hf present within the tertiary γ' precipitates. A constant level of Hf concentration was only seen some 80 nm from the γ'-γ interface. The proxigrams in Fig. 4 reveal compositional variations leading up to the γ' interface for Ti, Ta, Al and Mo. These trends in the profiles are consistent across all primary, secondary and tertiary γ', but are most apparent across the primary γ'-γ interface. With the exception of Mo, all of these elements are classified as γ'-stabilisers, residing on the β-lattice sites. However the spatial distribution maps of Fig. 6 show that for RR1000, Mo is also preferentially located in these β-lattice sites. This suggests that there may be competition for the finite number β-lattice sites leading up to the γ'-γ interface.

Kinetic effects likely contribute to the observed phase compositions. However, the lack of temperature dependence on the observed extended concentration profiles across the precipitate-matrix interfaces in Fig. 4b, together with the confinement of this behaviour to γ'-stabilising elements, suggests that some other factor is at work. Lattice misfit effects may play a significant role here. The lattice misfit (δ) between the γ/γ' regions is defined by:

$$\delta = 2\left[\frac{a_{\gamma'} - a_{\gamma}}{a_{\gamma'} + a_{\gamma}}\right]$$

where a_{γ} and $a_{\gamma'}$ terms correspond to the lattice spacings in the different phases. These in turn can be estimated from Vegard's Law, defined for the γ' phase as:

$$a_{\gamma'} = a_{\gamma}^0 + \sum_i \Gamma_i^{\gamma'} x_i^{\gamma'}$$

This term (along with an equivalent expression for the γ phase), demonstrates lattice parameters are related to the mole fractions of each solute species present (x), and to their Vegard coefficients (Γ), which is effectively a measure of the size discrepancy between each solute species and the solvent Ni atoms. For the elements demonstrating extended concentration profiles across the γ'-γ interface, the Vegard coefficients in a Ni₃Al phase decrease in the order: Hf > Ta > Ti > Mo [41]. This order is also consistent with the relative depletions in each respective element leading up to the γ'-γ interfaces in Fig. 4. Near the interface, the presence of the slightly

more compact γ phase prevents the lattice from deforming sufficiently in the γ′ phase to allow large species such as Hf to fit. This may also explain why so little Hf is observed in the tertiary precipitates; these are simply too small to allow for the lattice spacings to sufficiently relax to accommodate Hf, while some (but still less) Ti and Ta can be retained. Regardless of the mechanism, the deviation from expected chemistry at the γ′-γ boundaries may have important implications for predicting dislocation motion through the alloy.

4.3. Site occupancy behaviour

The preferences of elements to occupy specific γ′ lattice sites are summarised in Table 4. A number of studies have attempted to resolve the site preference of elements using combinations of first principles modelling, APT and XRD methods in a range of alloys. These often demonstrate strongly composition-dependent behaviour. For example in a model alloy it has been shown that Ta competes with W for β-lattice sites, to such an extent leading to complete reversal of W atom partitioning into the γ matrix [14]. For the elements in RR1000, relevant further examples of their behaviour in γ′ as measured/predicted within other known alloys are also included in Table 4. It is apparent that despite significant research there is still no consensus on lattice site preferences for certain species in γ′. For example, Mo prefers α-lattice sites in Rene88 [46], but strongly favours β-lattice sites in a model Ni-Al-Mo alloy [47] and in Ni₃Al [48]. In RR1000, while there is some Mo within the α-lattice sites, the majority clearly prefers the β-lattice site, Fig. 6b.

There are also discrepancies in the reported site preferences of Co and Cr, the most prevalent solutes in many Ni-based alloys. In RR1000, Co partitions strongly to α-lattice sites. The site preference is however predicted to be particularly composition dependent [48], switching to β-lattice sites at Ni mole fractions above 0.75. Below 0.72 it prefers the α-lattice sites, in agreement with the experimental data here (Ni mole fraction of 0.68). Cr also strongly prefers the α-lattice sites in RR1000. However a slight β-lattice preference is predicted in the Ni₃Al system [48], while in Rene88 there is no clear consensus - APT suggests the β-lattice, but synchrotron XRD indicates the α-lattice [46]. This discrepancy was attributed to the XRD fitting model relying on the limited amount of APT data, highlighting the difficulties in extracting site occupancies in small precipitates.

For Hf, which partitions strongly to γ′, all data in Table 4 indicates a preference for β-lattice sites. However, even for this element a recent APT study of two model alloys observed Hf partitioning to the γ matrix [49]. The authors attributed this to a low Co:Cr ratio; Cr increases the solubility of Hf in the γ matrix, while Co stabilises γ′ for Hf. Comparing the model ME-9 alloy with RR1000, the main difference is the Co γ′ content; for every Cr atom there are four Co atoms in RR1000, compared to just over two Co atoms in ME-9. Our results are therefore consistent with their explanation.

This discussion of site occupancies highlights the complex, strongly composition-dependent interaction between elements, and emphasises that verifying predictions made using model alloys against actual engineering materials is vital. New generation Ni-disc alloys currently being developed by gas-turbine manufacturers have a range of variations in Cr, Co and Mo; these will need to be examined directly to understand element partitioning and its consequences.

4.4. Grain boundary/boride chemistry

A single grain boundary along with an intragranular boride were also inspected by APT. Segregation of Cr, Mo, B and slight C enrichment was seen at a γ-γ grain boundary. B and C are introduced during processing as they strengthen grain boundaries, improving creep resistance, which is an active area of research [41]. However in excessive quantities they have potentially negative effects, forming continuous boride/carbide layers between boundaries which reduces strength. Only isolated boride/carbides were identified by SEM in RR1000; most were found as spherical particles within grains.

A prior APT study focussing solely on grain boundaries in an N18 superalloy showed similar enhancement of Mo and B at γ-γ grain boundaries [26]. Over the four such interfaces examined the average Γ values were 9.2 (Mo) and 8.3 (B) atoms/nm² for N18 containing 3.8 at.% Mo doped with 0.08 at.% B. We therefore see slightly more Mo segregation (11 atoms/nm²) and less B (5.6 atoms/nm²) in the current study, but the numbers are comparable. Carbon is also present in the N18 alloy (0.08 at.%), and while APT demonstrated very slight grain boundary segregation it was at a level insufficient to quantify. In the current work we detect traces (0.01 at.%) of C in the bulk, with no obvious γ/γ′ partitioning. At the grain boundary segregation of C is weak but detectable, indicating that B has a much stronger driving force to accumulate here. The same trend has also been noted on Inconel 718 [1], in which C competes with B at grain boundaries, illustrating a further interaction between trace species.

While Mo and Cr dominate the boride phase identified, there are also traces of Ti, Co, Ni and Ta. A recent study of boron doping in a new STAL15-CC polycrystalline superalloy also revealed M₅B₃ borides by APT, confirming the crystal structure by TEM [2]. In this alloy the Cr content is very similar to RR1000, but with only 0.6 at.% Mo compared with 3.2 at.% here. The Mo level we detect in the boride here is also much higher, 33.8 at.% compared to only 2.3 at.% in STAL15-CC. The composition of these phases is non-trivial, and worthy of further detailed separate studies, particularly if boride levels are raised in future alloys to enhance creep properties. The same is also true for dedicated examination of the relationship between grain boundary character and segregation levels. In the current work there is however no indication of Hf present at any point within the grain boundaries as intended; it is all caught up within the primary/secondary γ′ phases and carbides.

Table 4
Summary of site dependencies for selected elements in γ′ phases for current work and examples from literature on APT studies of engineering alloys (also including XRD) [46], a model ternary [47], a doped Ni₃Al [50] sample and from first principles calculations within Ni₃Al [48].

	Ni	Cr	Co	Mo	Al	Ti	Ta	Hf
RR1000	α	α	α	Mixed, mainly β	β	β	β	β
Rene88 [46]	α	α[a], β	No pref.	α[a]	β	β	–	–
Ni-Al-Mo [47]	α	–	–	β	β	–	–	–
Ni₃Al [50]	α	–	α	–	β	–	–	β
Ni₃Al (model) [48]	α	β	Comp. dependent	β	β	β	β	β

[a] XRD data-based measurement.

5. Conclusions

A detailed characterisation of individual elemental distributions within the commercially important superalloy RR1000 has been undertaken utilising Atom Probe Tomography, Scanning Electron Microscopy and thermodynamic modelling. Overall, the unique features identified in this alloy demonstrate it is vital that advanced techniques are used to understand fundamental behaviour for in-service materials. From this study we have made the following main observations:

- The composition of the γ' phases differs between the primary, secondary and in particular tertiary phases, a result which is not in complete agreement with ThermoCalc modelling.
- At the γ'-γ phase boundaries, the chemistry within the γ' regions deviates further from expectations, particularly for Hf, Ti and Ta. This may have important implications for dislocation motion at such boundaries.
- Tertiary γ' precipitate composition is uniform across 4—20 nm in size.
- RR1000 demonstrates unique site occupancies for Mo, Co and Cr in the γ' phase, not in accordance with observations on simpler model alloys.
- The γ—γ grain boundary chemistry is markedly different than the matrix, with a large Gibbsian interfacial excess of Mo $(11.0 \pm 0.2$ atoms/nm$^2)$ and B $(5.6 \pm 0.6$ atoms/nm$^2)$.
- Grain boundary and intragranular borides are present, with an M_5B_3 structure mainly containing Mo and Cr, along with trace levels of Ti, Ni, Co and Ta. No Hf is present at all at the grain boundary, at variance with expectations. Smaller intragranular Ta-Hf rich carbides are also detected.

Acknowledgements

References

[1] T. Alam, P.J. Felfer, M. Chaturvedi, L.T. Stephenson, M.R. Kilburn, J.M. Cairney, Segregation of B, P, and C in the Ni-Based superalloy, inconel 718, Metall. Mater. Trans. A 43 (2012) 2183—2191, http://dx.doi.org/10.1007/s11661-012-1085-9.

[2] P. Kontis, H.A. Yusof Mohd, S. Pedrazzini, K.L. Moore, P.A.J. Bagot, M.P. Moody, et al., On the effect of boron on grain boundary character in a new polycrystalline superalloy, Acta Mater. 103 (2016) 688—699.

[3] J.X. Dong, X.S. Xie, R.G. Thompson, The influence of sulfur on stress-rupture fracture in inconel 718 superalloys, Metall. Mater. Trans. A 31 (2000) 2135—2144, http://dx.doi.org/10.1007/s11661-000-0131-1.

[4] M.A. Smith, W.E. Frazier, B.A. Pregger, Effect of sulfur on the cyclic oxidation behavior of a single crystalline, nickel-base superalloy, Mater. Sci. Eng. A A203 (1995) 388—398.

[5] T.M.T. Pollock, S. Tin, Nickel-based superalloys for advanced turbine engines: chemistry, microstructure and properties, J. Propuls. Power 22 (2006) 361—374, http://dx.doi.org/10.2514/1.18239.

[6] F. Tancret, H.K.D.H. Bhadeshia, D.J.C. MacKay, Design of a creep resistant nickel base superalloy for power plant applications: Part 1-Mechanical properties modelling, Mater. Sci. Technol. 19 (2003) 283—290.

[7] L.Z. He, Q. Zheng, X.F. Sun, H.R. Guan, Z.Q. Hu, A.K. Tieu, et al., High temperature low cycle fatigue behavior of Ni-base superalloy M963, Mater. Sci. Eng. A 402 (2005) 33—41, http://dx.doi.org/10.1016/j.msea.2005.03.105.

[8] C. Stöcker, M. Zimmermann, H.-J. Christ, Z.-L. Zhan, C. Cornet, L.G. Zhao, et al., Microstructural characterisation and constitutive behaviour of alloy RR1000 under fatigue and creep—fatigue loading conditions, Mater. Sci. Eng. A 518 (2009) 27—34, http://dx.doi.org/10.1016/j.msea.2009.04.055.

[9] L. Whitmore, H. Leitner, E. Povoden-Karadeniz, R. Radis, M. Stockinger, Transmission electron microscopy of single and double aged 718Plus superalloy, Mater. Sci. Eng. A 534 (2012) 413—423, http://dx.doi.org/10.1016/j.msea.2011.11.089.

[10] O. Paris, M. Fährmann, E. Fährmann, T.M. Pollock, P. Fratzl, Early stages of precipitate rafting in a single crystal NiAlMo model alloy investigated by small-angle X-ray scattering and TEM, Acta Mater. 45 (1997) 1085—1097, http://dx.doi.org/10.1016/S1359-6454(96)00223-6.

[11] E.W. Huang, P.K. Liaw, L. Porcar, Y. Liu, Y.L. Liu, J.J. Kai, et al., Study of nano-precipitates in a nickel-based superalloy using small-angle neutron scattering and transmission electron microscopy, Appl. Phys. Lett. 93 (2008) 1—4, http://dx.doi.org/10.1063/1.3002288.

[12] D. Blavette, E. Cadel, B. Deconihout, The role of the atom probe in the study of nickel-based superalloys, Mater. Charact. 44 (2000) 133—157.

[13] M.K. Miller, Contributions of atom probe tomography to the understanding of nickel-based superalloys, Micron 32 (2008) 757—764.

[14] Y. Amouyal, Z. Mao, D.N. Seidman, Combined atom probe tomography and first-principles calculations for studying atomistic interactions between tungsten and tantalum in nickel-based alloys, Acta Mater. 74 (2014) 296—308, http://dx.doi.org/10.1016/j.actamat.2014.03.064.

[15] J.Y. Hwang, S. Nag, A.R.P. Singh, R. Srinivasan, J. Tiley, G.B. Viswanathan, et al., Compositional variations between different generations of γ' precipitates forming during continuous cooling of a commercial nickel-base superalloy, Metall. Mater. Trans. A Phys. Metall. Mater. Sci. 40 (2009) 3059—3068, http://dx.doi.org/10.1007/s11661-009-0075-z.

[16] D.M. Collins, B.D. Conduit, H.J. Stone, M.C. Hardy, G.J. Conduit, R.J. Mitchell, Grain growth behaviour during near-γ' solvus thermal exposures in a polycrystalline nickel-base superalloy, Acta Mater. 61 (2013) 3378—3391, http://dx.doi.org/10.1016/j.actamat.2013.02.028.

[17] A. Prakash, J. Gue, Atom probe informed simulations of dislocation — precipitate interactions reveal the importance of local interface curvature, Acta Mater. 92 (2015) 33—45, http://dx.doi.org/10.1016/j.actamat.2015.03.050.

[18] J. Rüsing, N. Wanderka, U. Czubayko, V. Naundorf, D. Mukherji, J. Rösler, Rhenium distribution in the matrix and near the particle — matrix interface in a model Ni—Al—Ta—Re superalloy, Scr. Mater. 46 (2002) 235—240.

[19] A. Mottura, N. Warnken, M.K. Miller, M.W. Finnis, R.C. Reed, Atom probe tomography analysis of the distribution of rhenium in nickel alloys, Acta Mater. 58 (2010) 931—942, http://dx.doi.org/10.1016/j.actamat.2009.10.008.

[20] E. Fleischmann, M.K. Miller, E. Affeldt, U. Glatzel, Quantitative experimental determination of the solid solution hardening potential of rhenium, tungsten and molybdenum in single-crystal nickel-based superalloys, Acta Mater. 87 (2015) 350—356, http://dx.doi.org/10.1016/j.actamat.2014.12.011.

[21] R.C. Reed, A.C. Yeh, S. Tin, S.S. Babu, M.K. Miller, Identification of the partitioning characteristics of ruthenium in single crystal superalloys using atom probe tomography, Scr. Mater. 51 (2004) 327—331, http://dx.doi.org/10.1016/j.scriptamat.2004.04.019.

[22] J.S. Van Sluytman, A. La Fontaine, J.M. Cairney, T.M. Pollock, Elemental partitioning of platinum group metal containing Ni-base superalloys using electron microprobe analysis and atom probe tomography, Acta Mater. 58 (2010) 1952—1962, http://dx.doi.org/10.1016/j.actamat.2009.11.038.

[23] Y. Zhou, D. Isheim, G. Hsieh, Effects of ruthenium on phase separation in a model Ni-Al-Cr-Ru superalloy, Philos. Mag. 93 (2013) 1326—1350, http://dx.doi.org/10.1080/14786435.2013.765989.

[24] K. Matuszewski, R. Rettig, H. Matysiak, Z. Peng, I. Povstugar, P. Choi, et al., Effect of ruthenium on the precipitation of topologically close packed phases in Ni-based superalloys of 3rd and 4th generation, Acta Mater. 95 (2015) 274—283.

[25] Y. Xu, Q. Ran, J. Li, J. Peng, X. Xiao, X. Cao, et al., Materials science & engineering a strengthening behavior of Nb in the modified nimonic 80A, Mater. Sci. Eng. A 569 (2013) 27—40, http://dx.doi.org/10.1016/j.msea.2013.01.043.

[26] D. Lemarchand, E. Cadel, S. Chambreland, D. Blavette, Investigation of grain-boundary structure-segregation relationship in an N18 nickel-based superalloy, Philos. Mag. A 82 (2002) 1651—1669, http://dx.doi.org/10.1080/01418610210125783.

[27] L. Viskari, K. Stiller, Atom probe tomography of Ni-base superalloys Allvac 718Plus and Alloy 718, Ultramicroscopy 111 (2011) 652—658, http://dx.doi.org/10.1016/j.ultramic.2011.01.015.

[28] H.S. Kitaguchi, M.P. Moody, H.Y. Li, H.E. Evans, M.C. Hardy, S. Lozano-Perez, An atom probe tomography study of the oxide — metal interface of an oxide intrusion ahead of a crack in a polycrystalline Ni-based superalloy, Scr. Mater. 97 (2015) 41—44, http://dx.doi.org/10.1016/j.scriptamat.2014.10.025.

[29] L. Viskari, M. Hörnqvist, K.L.L. Moore, Y. Cao, K. Stiller, Intergranular crack tip oxidation in a Ni-base superalloy, Acta Mater. 61 (2013) 3630—3639, http://dx.doi.org/10.1016/j.actamat.2013.02.050.

[30] D.H. Ping, C.Y. Cui, Y.F. Gu, H. Harada, Microstructure of a newly developed γ' strengthened Co-base superalloy, Ultramicroscopy 107 (2007) 791—795, http://dx.doi.org/10.1016/j.ultramic.2007.02.010.

[31] S. Meher, H.Y. Yan, S. Nag, D. Dye, R. Banerjee, Solute partitioning and site preference in γ/γ' cobalt-base alloys, Scr. Mater. 67 (2012) 850—853, http://dx.doi.org/10.1016/j.scriptamat.2012.08.006.

[32] M. Knop, P. Mulvey, F. Ismail, A. Radecka, K.M. Rahman, T.C. Lindley, et al., A new polycrystalline Co-Ni superalloy, J. Mater. 66 (2014) 2495—2501, http://dx.doi.org/10.1007/s11837-014-1175-9.

[33] M. Naeem, R. Singh, D. Probert, Implications of engine deterioration for a high-pressure turbine-blade's low-cycle fatigue (LCF) life-consumption, Int. J. Fatigue 21 (1999) 831—847, http://dx.doi.org/10.1016/S0142-1123(99)00025-0.

[34] D.W. Saxey, J.M. Cairney, D. McGrouther, T. Honma, S.P. Ringer, Atom probe specimen fabrication methods using a dual FIB/SEM, Ultramicroscopy 107 (2007) 756—760, http://dx.doi.org/10.1016/j.ultramic.2007.02.024.

[35] R.J. Mitchell, M.C. Hardy, M. Preuss, S. Tin, Development of γ' morphology in P/M rotor disc alloys during heat treatment, Superalloys 2004 (2004) 361—370.

[36] D.M. Collins, H.J. Stone, A modelling approach to yield strength optimisation in a nickel-base superalloy, Int. J. Plast. 54 (2014) 96—112.

[37] T. Boll, T. Al-Kassab, Y. Yuan, Z.G. Liu, Investigation of the site occupation of atoms in pure and doped TiAl/Ti3Al intermetallic, Ultramicroscopy 107 (2007) 796—801, http://dx.doi.org/10.1016/j.ultramic.2007.02.011.

[38] B. Gault, M.P. Moody, J.M. Cairney, S.P. Ringer, Atom Probe Microscopy, Springer, 2012.

[39] M.K. Miller, G.D.W. Smith, Atom probe analysis of interfacial segregation, Appl. Surf. Sci. 87—88 (1995) 243—250, http://dx.doi.org/10.1016/0169-4332(94)00493-5.

[40] M.L. Taheri, J.T. Sebastian, B.W. Reed, D.N. Seidman, A.D. Rollett, Site-specific atomic scale analysis of solute segregation to a coincidence site lattice grain boundary, Ultramicroscopy 110 (2010) 278—284, http://dx.doi.org/10.1016/j.ultramic.2009.11.006.

[41] R.C. Reed, The Superalloys — Fundamentals and Applications, Cambridge University Press, 2006.

[42] Y.Q. Chen, T.J.A. Slater, E.A. Lewis, E.M. Francis, M.G. Burke, M. Preuss, et al., Measurement of size-dependent composition variations for gamma prime (γ') precipitates in an advanced nickel-based superalloy, Ultramicroscopy 144 (2014) 1—8, http://dx.doi.org/10.1016/j.ultramic.2014.04.001.

[43] S.H. Liu, C.P. Liu, W.Q. Liu, X.N. Zhang, Y. Pan, C.Y. Wang, Investigation of the elemental partitioning behaviour and site preference in ternary model nickel-based superalloys by atom probe tomography and first-principles calculations, Philos. Mag. 96 (2016) 2204—2218.

[44] C. Booth-Morrison, Z. Mao, R.D. Noebe, D.N. Seidman, Chromium and tantalum site substitution patterns in Ni3Al (L 12) γ' -precipitates, Appl. Phys. Lett. 93 (2008) 3—6, http://dx.doi.org/10.1063/1.2956398.

[45] D.M. Collins, L. Yan, E.A. Marquis, L.D. Connor, J.J. Ciardiello, A.D. Evans, et al., Lattice misfit during ageing of a polycrystalline nickel-base superalloy, Acta Mater. 61 (2013) 7791—7804, http://dx.doi.org/10.1016/j.actamat.2013.09.018.

[46] J.S. Tiley, O. Senkov, G. Viswanathan, S. Nag, J. Hwang, R. Banerjee, A methodology for determination of γ' site occupancies in nickel superalloys using atom probe tomography and X-ray diffraction, Metall. Mater. Trans. A 44 (2013) 31—38, http://dx.doi.org/10.1007/s11661-012-1456-2.

[47] Y. Tu, Z. Mao, D.N. Seidman, Phase-partitioning and site-substitution patterns of molybdenum in a model Ni-Al-Mo superalloy: an atom-probe tomographic and first-principles study, Appl. Phys. Lett. 101 (2012), http://dx.doi.org/10.1063/1.4753929.

[48] C. Jiang, B. Gleeson, Site preference of transition metal elements in Ni3Al, Scr. Mater. 55 (2006) 433—436, http://dx.doi.org/10.1016/j.scriptamat.2006.05.016.

[49] Y. Amouyal, D.N. Seidman, The role of hafnium in the formation of misoriented defects in Ni-based superalloys: an atom-probe tomographic study, Acta Mater. 59 (2011) 3321—3333, http://dx.doi.org/10.1016/j.actamat.2011.02.006.

[50] M.K. Miller, J.A. Horton, Site occupation determinations by APFIM for Hf, Fe, and Co in Ni3Al, Scr. Metall. 20 (1986) 1125—1130, http://dx.doi.org/10.1016/0036-9748(86)90188-2.